Journal of Alloys and Metallurgical Systems 7 (2024) 100101

Contents lists available at ScienceDirect

Journal of Alloys and Metallurgical Systems

journal homepage: www.journals.elsevier.com/journal-of-alloys-and-metallurgical-systems

Regulating of wear properties through microstructure engineering in novel cost-effective $Fe_{30}Ni_{25}Cr_{25}Mo_{10}Al_{10}$ high-entropy alloy processed by cyclic closed-die forging

Majid Naseri [a,*], Alena Myasnikova [a], Davood Gholami [b], Omid Imantalab [c,*], Dmitry Mikhailov [a], Mostafa Amra [d], Nataliya Shaburova [a], Milena Efimova [a], Aleksandr Orlov [a], Seyedmehdi Hosseini [e], Yong-Cheng Lin [f], Abdel-Hamid I. Mourad [g,h], Evgeny Trofimov [a]

[a] South Ural State University, 76 Lenin Av., Chelyabinsk 454080, Russia
[b] School of Metallurgy and Materials Engineering, Iran University of Science and Technology, Tehran, Iran
[c] Department of Materials Engineering, Faculty of Engineering, Bu-Ali Sina University, Hamedan, Iran
[d] Padideh Sanat Ouj Co., Tehran, Iran
[e] Brunel Centre for Advanced Solidification Technology (BCAST), Brunel University London, Uxbridge UB8 3PH, UK
[f] School of Mechanical and Electrical Engineering, Central South University, Changsha 410083, China
[g] Mechanical and Aerospace Engineering Department, College of Engineering, United Arab Emirates University, Al-Ain 15551, United Arab Emirates
[h] National Water and Energy Center, United Arab Emirates University, Al-Ain 15551, United Arab Emirates

ARTICLE INFO

Keywords:
Cost-effective high-entropy alloy
Cyclic closed-die forging
Microstructure characterization
Crystallographic texture
Hardness
Wear resistance

ABSTRACT

This study presents a novel cost-effective $Fe_{30}Ni_{25}Cr_{25}Mo_{10}Al_{10}$ high-entropy alloy with a dual-phase microstructure that was processed using cyclic closed-die forging (CCDF) at room temperature for a maximum of six passes. The as-homogenized alloy exhibited [CrMoFe]-rich dendrites with dual-size morphology dispersed in an almost uniform face-centered cubic (FCC) matrix. It was found that as the number of CCDF passes increased, leading to a more homogenous nanograin, there was an accumulation of dislocations, fragmentation of [CrMoFe]-rich dendrites, and enhanced distribution within the matrix. These conditions were conducive to the creation of a nanostructured $Fe_{30}Ni_{25}Cr_{25}Mo_{10}Al_{10}$ alloy with superior mechanical properties. Texture analysis indicated that the prominent texture components for the $Fe_{30}Ni_{25}Cr_{25}Mo_{10}Al_{10}$ alloy after six passes were Rotated Cube {001}<110>, S {123}<634>, and Dillamore {4 4 11}<11 11 8>. After the sixth CCDF pass, the $Fe_{30}Ni_{25}Cr_{25}Mo_{10}Al_{10}$ alloy exhibited the highest microhardness (~ 974 HV) and the lowest wear rate (~ $(0.8 \pm 0.1) \times 10^{-5}$ $mm^3.N^{-1}.m^{-1}$). Additionally, it was proposed that the development of the Rotated Cube {001}<110> texture component contributed positively to enhancing wear resistance in the cost-effective high-entropy alloys. Considering the obtained results, it is reasonable to propose that CCDF processing is significant potential for the advancement of cost-effective nanostructured high-entropy alloys for industrial applications.

1. Introduction

High-entropy alloys (HEAs) or multi-principal element alloys (MPEAs) first reported in 2004 have captured the interest of materials scientists due to their exceptional properties such as good corrosion resistance, excellent low-temperature ductility, and high-temperature characteristics [1–4]. The concept of HEAs originally referred to equiatomic multi-principal element alloy with a single-phase solid solution and was initially defined as alloys containing at least five principal elements in an equiatomic proportions [5–9]. The current definition of HEAs has expanded to include non-equiatomic alloys with multiple phases or minor additions, aiming to encompass a broader range of HEAs with significantly improved properties [10–13]. Lu et al. [14] proposed the concept of eutectic high-entropy alloys (EHEAs) in 2014, which combine the advantages of HEAs and eutectic alloys. The features of low melting point and no liquid-solid mixing zone solve the problems of poor castability and serious composition segregation of HEAs, which improved the matching of strength and plasticity of conventional HEAs. Subsequently, the Co element is so expensive, which hampers the industrialization of HEAs. Therefore, many researchers

* Corresponding authors.
E-mail addresses: majid_na3ri@yahoo.com, naserim@susu.ru (M. Naseri), o.imantalab@basu.ac.ir (O. Imantalab).

https://doi.org/10.1016/j.jalmes.2024.100101
Received 29 June 2024; Received in revised form 6 August 2024; Accepted 14 August 2024
Available online 15 August 2024

have designed Co-free EHEAs, such as FeNiCrMo [15], $Al_xCrFeNi$ [16], and $CrFeNiNb_{0.31}$ [17].

Due to the effectiveness of the integrated strengthening mechanisms, non-equiatomic HEAs with multi-phases often exhibit superior mechanical characteristics compared to equiatomic single-phase HEAs. Non-equiatomic HEAs typically consist of a supersaturated metastable solid solution matrix and intermetallic compounds at specific temperatures [18–21]. This results in a higher potential for significant grain refinement through severe plastic deformation (SPD) processing, surpassing that of both traditional alloys and equiatomic HEAs composed of stable single phases. However, most reported HEAs are nearly equiatomic and contain large concentrations of expensive metals such as Co or Mo [22–27]. A major obstacle hindering the industrial applications of these metallic materials is the high cost of near-equiaxial HEAs currently available. Therefore, overcoming the challenges associated with designing and implementing HEAs in industrial applications necessitates the development of cost-effective Fe-enriched HEAs with outstanding mechanical properties.

Thermomechanical processing, including plastic deformation processes, thermal processes, and SPD are the most efficient methods for achieving ultrafine-grained (UFG, average grain size 0.1–1 μm) or nanocrystalline (NC, average grain size $\leq$ 0.1 μm) materials in metals and alloys [28–34]. For example, Otto et al. [35] studied the tensile properties of the CoCrFeMnNi Cantor alloy in relation to temperature and grain size. After homogenization and thermomechanical processing involving cold rolling and recrystallized annealing, single-phase microstructures with grain sizes ranging from 4 to 160 μm were obtained. Tensile tests revealed that refining the grain size from 160 to 4 μm significantly increased the yield strength at temperatures up to 873 K. Current literature indicates that common SPD techniques used in HEAs include equal-channel angular pressing/extrusion (ECAP/ECAE) [26, 36–38] and high-pressure torsion (HPT) [27,39–41]. Another prevalent SPD technique for grain refinement in difficult-to-deform alloys such as Mg alloys is cyclic closed-die forging (CCDF) [42–44]. The CCDF technique, developed by Ghosh et al. [45], involves cyclic compression of a billet with dimensions of H × W (height × width) inside a rectangular channel, resulting in a reduction of height by up to 50 % (Fig. 1). The equivalent deformation (ε_{eq}) achieved in this process can be estimated using Eq. (1).

$$\varepsilon_{eq} = N\frac{2}{\sqrt{3}}Ln\left(\frac{H}{W}\right) \quad (1)$$

where N is the number of passes, H is the height, and W is the width of the specimen. It is important to note that the CCDF induces higher strains per pass compared to other SPD processes, and may lead to a more uniform material structure due to multi-directional deformation. Consequently, considering CCDF as a promising approach with the potential to achieve exceptional properties in HEAs is justifiable.

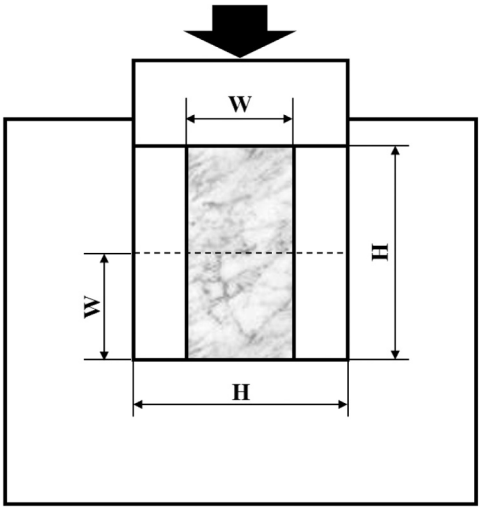

Fig. 1. The schematic representation of the CCDF processing technique.

The lack of systematic research on developing cost-effective nanostructured high-entropy alloys (NsHEAs) with superior properties through CCDF processing motivated the authors to conduct this study. This study is, to our knowledge, the first to investigate the regulation of wear properties through microstructure engineering in a novel cost-effective Fe-enriched high-entropy alloy processed by CCDF. The motivation for this research stems from the recognized impact of CCDF on a novel low-cost $Fe_{30}Ni_{25}Cr_{25}Mo_{10}Al_{10}$ alloy, featuring a face-centered cubic-based metallic matrix and [CrMoFe]-rich dendrite phase designed using the computer coupling of phase diagrams and thermochemistry (CALPHAD) method.

2. Experimental procedures

The Fe-rich non-equiatomic high-entropy alloy ($Fe_{30}Ni_{25}Cr_{25}Mo_{10}Al_{10}$) ingot was initially prepared through vacuum melting the constituent elements with 99.9 wt% purity at temperatures ranging from 1873 to 1923 K. Subsequently, the Fe-rich alloy ingot (35 mm in diameter and 50 mm in height) was homogenized at 1173 K for 10 hours in a furnace and then air-quenched. The heat treatment was intended to homogenize the microstructure and relieve the residual stresses present in the samples prior to any process. The alloy was then cut into billets measuring approximately 30^{L} mm × 30^{W} mm × 20^{H} mm and subjected to CCDF at room temperature for six passes, accumulating a total equivalent strain of 4.80 (0.8 for each pass of CCDF).

The microstructure of the $Fe_{30}Ni_{25}Cr_{25}Mo_{10}Al_{10}$ alloy was analyzed using multiple techniques: (i) X-ray diffraction (XRD, Rigaku, Japan) using monochromatic CuKα radiation; (ii) field emission scanning electron microscope (FE-SEM, JEOL JSM7001F, Japan) equipped with energy dispersive spectroscopy (EDS, Oxford INCA X-max 80, Oxford Instruments, Great Britain); and (iii) electron backscatter diffraction (EBSD) integrated with the FE-SEM (Philips XL30). EBSD data was processed with HKL Channel 5 software.

Hardness was measured using an FM-800 Vickers microhardness tester with a 300 g load and a 15 s dwell time. Wear tests were performed on the as-homogenized and CCDF-processed specimens at room temperature using a pin-on-disc wear test machine. Cylindrical pins, 20 mm in length and 5 mm in diameter, machined from as-forged billets, slide against the counterface of a hardened disk of steel AISI 52100 measuring 100 mm in diameter and having a hardness of 62–65 HRC. The axis of the pins was perpendicular to the direction of tool travel. The wear test included a sliding distance of 500 m, a normal force of 24 N, and a sliding velocity of 0.24 m/s. During the test, the friction coefficient was continuously and automatically recorded as a function of sliding time (distance). Each specimen underwent three trials, and the average value was reported. Subsequently, the surface morphologies of the worn areas, without removing any surface debris, were examined using a field emission scanning electron microscope (FE-SEM, MIRA TESCAN).

3. Results and discussion

The XRD patterns of the as-homogenized $Fe_{25}Ni_{25}Cr_{25}Mo_{25}$ and $Fe_{30}Ni_{25}Cr_{25}Mo_{10}Al_{10}$ alloys are presented in Fig. 2. In the equiatomic $Fe_{25}Ni_{25}Cr_{25}Mo_{25}$ alloy, a predominantly single face-centered cubic (FCC) phase is observed. In contrast, the non-equiatomic $Fe_{30}Ni_{25}Cr_{25}Mo_{10}Al_{10}$ alloy exhibits a dual-phase structure consisting of FCC as the primary phase and the σ phase ($Cr_{0.22}Mo_{0.18}Fe_{0.6}$ type) with a body-centered tetragonal (BCT) structure as the secondary phase. Furthermore, the diffraction intensities of the major peaks corresponding to the FCC phase are significantly higher than those of the BCT phase, indicating the predominance of the FCC phase.

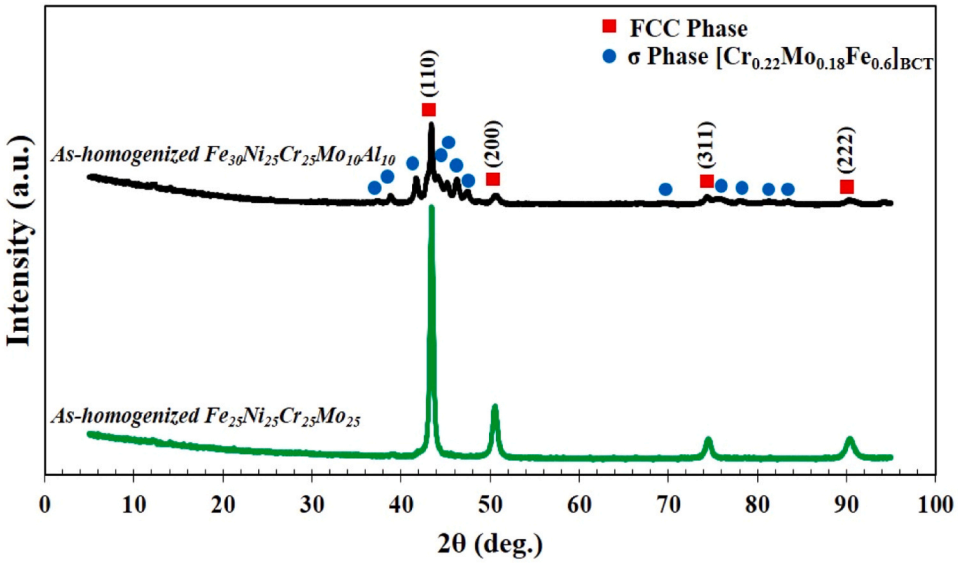

Fig. 2. XRD pattern of the as-homogenized $Fe_{25}Ni_{25}Cr_{25}Mo_{25}$ and Fe30Ni25Cr25Mo10Al10 alloys.

Fig. 3 shows the microstructure and EDS maps of the as-homogenized $Fe_{25}Ni_{25}Cr_{25}Mo_{25}$ and $Fe_{30}Ni_{25}Cr_{25}Mo_{10}Al_{10}$ alloys. The EDS results shown in Table 1 further validate the phases identified by XRD. In Fig. 3 (a), the microstructure of the as-homogenized $Fe_{25}Ni_{25}Cr_{25}Mo_{25}$ alloy reveals a single FCC structure. Additionally, grain boundaries can be observed with a mean grain size of approximately 50 μm. Fig. 3(b) illustrates that the microstructure of the $Fe_{30}Ni_{25}Cr_{25}Mo_{10}Al_{10}$ alloy is composed of [CrMoFe]-rich dark-gray dendrites with dual-size distributed within a nearly homogenous high-entropy alloy matrix, appearing as a bright-gray region in the back-scattered electron SEM (BSE-SEM) image. The EDS analysis confirms that the FCC phase in the alloy contains Fe, Ni, Cr, Mo, and Al, while the dark-gray dendrite phase contains Fe, Cr, and Mo. The FCC phase exhibits higher Fe and Ni content compared to the dark-gray dendrite phase. Previous studies [46,47] have shown that a single FCC phase formation requires an average valence electron concentration (VEC) exceeding eight in a high-entropy alloy. Therefore, it can be concluded that the FCC phase represents a Fe-Ni enriched solid solute, while the [CrMoFe]-rich phase corresponds to an intermetallic compound, consistent with the XRD results.

A practical approach to reduce the cost of HEAs is to avoid the use of

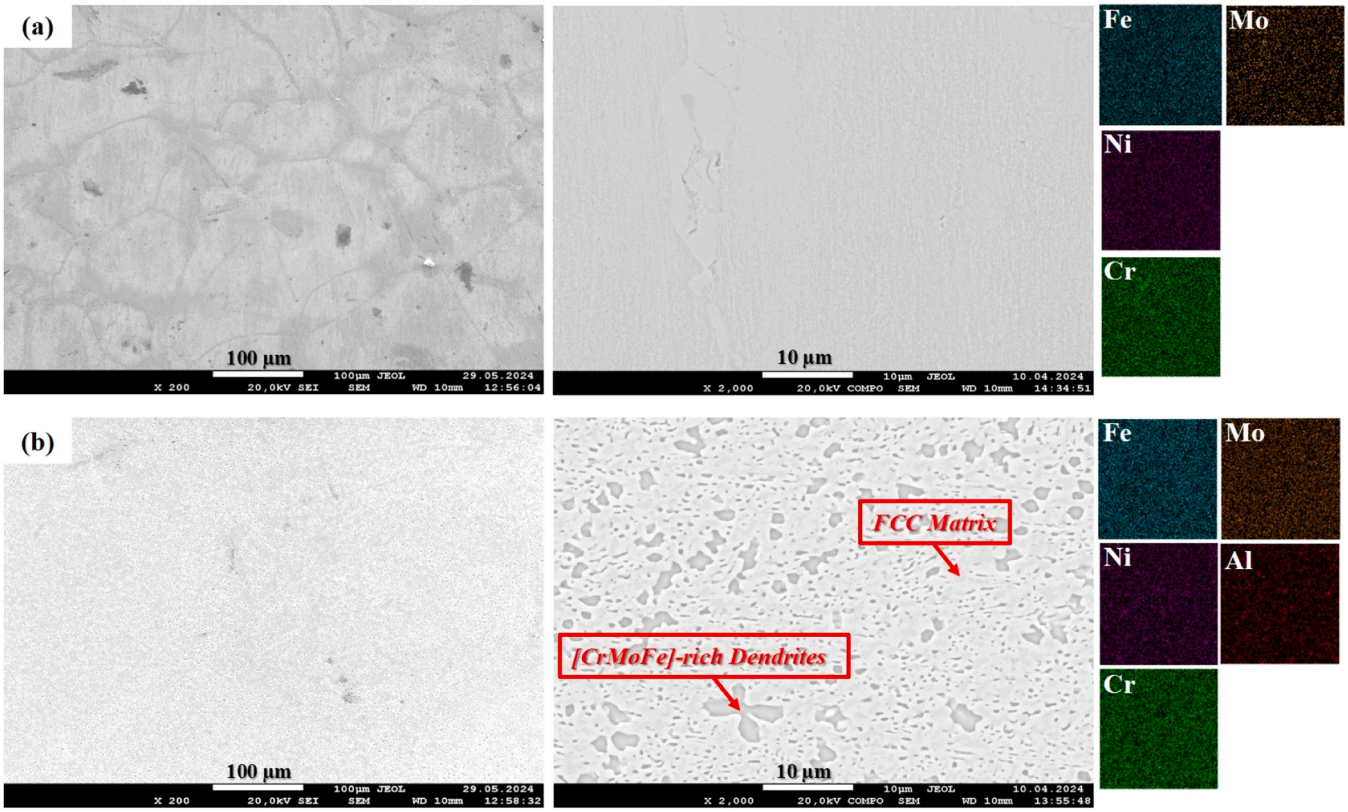

Fig. 3. SEM image and the corresponding EDS maps of the as-homogenized (a) $Fe_{25}Ni_{25}Cr_{25}Mo_{25}$ and (b) $Fe_{30}Ni_{25}Cr_{25}Mo_{10}Al_{10}$ alloys.

Table 1
Chemical composition of the as-homogenized $Fe_{25}Ni_{25}Cr_{25}Mo_{25}$ and $Fe_{30}Ni_{25}Cr_{25}Mo_{10}Al_{10}$ alloys. Av – average composition; D – dendrite; ID – interdendritic space.

	Phase, XRD		Fe	Ni	Cr	Mo	Al
$Fe_{25}Ni_{25}Cr_{25}Mo_{25}$	FCC	Av	27.55	25.92	27.91	18.63	—
$Fe_{30}Ni_{25}Cr_{25}Mo_{10}Al_{10}$	FCC+$[CrMoFe]_{BCT}$	Av	32.88	24.52	29.23	6.96	6.41
		D	28.54	18.59	33.80	15.46	3.61
		ID	38.64	28.91	20.14	5.94	6.37

expensive Co, which is commonly utilized in HEAs. By adjusting the Fe/Ni to Cr/Mo ratio, the composition of HEAs can be tailored. In the present study, the Fe to Mo ratio was increased to achieve the dual-phase structure comprising of FCC and the intermetallic phases in the FeNiCrMo alloy system (see Figs. 2 and 3), as Fe is more cost-effective compared to other elements while Mo is the most expensive. Moreover, this novel alloy exhibits elevated concentrations of Cr and Al, along with a complex structure that holds promise for high-temperature applications. Consequently, it is expected that the proposed Fe-enriched $Fe_{30}Ni_{25}Cr_{25}Mo_{10}Al_{10}$ alloy, particularly when processed using CCDF, will demonstrate superior mechanical characteristics at ambient temperature.

Fig. 4 displays the EBSD inverse pole figure (IPF) maps and misorientation angle distribution of the $Fe_{30}Ni_{25}Cr_{25}Mo_{10}Al_{10}$ alloy following successive CCDF passes. In Fig. 4(a), the IPF map illustrates the microstructure of the as-homogenized $Fe_{30}Ni_{25}Cr_{25}Mo_{10}Al_{10}$ alloy, with fine [CrMoFe]-rich phases and coarsened FCC structures. The average misorientation angle of the boundaries, the proportion of high-angle grain boundaries, and the grain size in the as-homogenized $Fe_{30}Ni_{25}Cr_{25}Mo_{10}Al_{10}$ alloy are 29.53°, 72 %, and 35 μm, respectively. Subsequent to two CCDF passes, a reduction in grain size is observed, as shown in Fig. 4(b). The altered microstructure displays deformed grains with dislocation tangles, signifying substantial differences compared to the initial homogenized state. Following four passes (Fig. 4(c)), an increase in the dominance of high-angle grain boundaries is evident due to the improved microstructure uniformity, with the misorientation parameter rising to 34.43°, indicating continuous and discontinuous recrystallization. After six CCDF passes (Fig. 4(d)), all grains exhibit an equiaxed morphology, accompanied by an augmented fraction of ultrafine-grained regions. The average grain size of these equiaxed recrystallized grains is about 230 nm. Notably, after six passes, the CCDF-treated alloy exhibits an average misorientation of 36.27° and a high-angle grain boundary fraction of 82 %.

Fig. 5 illustrates the {111} pole figure (PF) of the $Fe_{30}Ni_{25}Cr_{25}Mo_{10}Al_{10}$ alloy following various CCDF passes. Fig. 5(a) shows Cube {100}<100> and A {110}<111> components with maximum intensities of 1.4 × R and 1.2 × R, respectively, potentially indicating the recrystallized state in the as-homogenized alloy. Following the two CCDF passes (Fig. 5(b)), the Cube {100}<100> component disappears, while the Brass {110}<221>, Copper {112}<111>, and Dillamore {4 4 11}<11 11 8> components emerge. The primary texture components include Brass {110}<221>, Copper {112}<111>, Dillamore {4 4 11}<11 11 8>, and A {110}<111> with the maximum intensities of 1.4 × R, 1.3 × R, 1.2 × R, and 1.0 × R, respectively. As depicted in Fig. 5(c), after four passes, the textural components are entirely analogous to those of the two-pass specimen. The dominant texture components are Brass {110}<221>, Copper {112}<111>, Dillamore {4 4 11}<11 11 8>, and Cube {100}<100> with the maximum intensities of 5.3 × R, 3.2 × R, 2.7 × R, and 1.1 × R, respectively. The total intensity of the components after the fourth pass displayed a remarkable increase compared to the earlier passes. Lastly, following six CCDF passes (Fig. 5(d)), the principal texture components are Rotated Cube {001}<110>, S {123}<634>, and Dillamore {4 4 11}<11 11 8> with the maximum intensities of 2.7 × R, 2.2 × R, and 1.3 × R, respectively.

The remarkable evolution of these components is attributed to the induction of high-angle grain boundaries by CCDF. These boundaries subdivide the grains with geometrically necessary dislocations (GND) before recrystallization, leading to the formation of equilibrium grain boundaries [48–53]. Also, the fractured fragments of [CrMoFe]-rich dendrites and nano shear bands in the microstructure can serve as nucleation sites for continuous recrystallization [54–58]. Therefore, the redundant shear strain and dynamic recrystallization during high CCDF passes facilitate the formation of equiaxed nanograins. This study demonstrates that the microstructure of the sixth pass significantly indicates the nanograin formation, due to the uniform distribution of fractured [CrMoFe]-rich dendrites, redundant shear strain, and continuous recrystallization. Consequently, it is expected that the intensity of major texture components, such as Rotated Cube {001}<110>, S {123}<634>, and Dillamore {4 4 11}<11 11 8>, will be either saturated or decreased.

Microhardness, wear rate, and friction coefficient data for the as-homogenized $Fe_{40}Ni_{25}Cr_{25}Mo_{25}$ alloy, as-homogenized $Fe_{30}Ni_{25}Cr_{25}Mo_{10}Al_{10}$ alloy, and the CCDF-processed alloy after six passes are summarized in Table 2 and Fig. 6. The as-homogenized $Fe_{25}Ni_{25}Cr_{25}Mo_{25}$ alloy with a single FCC phase exhibited the lowest hardness at 195 HV. Meanwhile, the as-homogenized $Fe_{30}Ni_{25}Cr_{25}Mo_{10}Al_{10}$ alloy with a dual-phase structure hardness displayed a hardness of 415 HV. As illustrated in Table 2, the microhardness of the CCDF-processed $Fe_{30}Ni_{25}Cr_{25}Mo_{10}Al_{10}$ alloy is higher than that of the as-homogenized state, which aligns with findings from previous studies on HPT or ECAP/ECAE-processed HEAs [23,26,41]. Specifically, the microhardness of the CCDF-processed alloy increased by 137 %, rising from 415 HV (for an as-homogenized composition) to 974 HV. This significant increase in hardness can be attributed to several mechanisms, such as solid solution hardening, Hall-Petch strengthening by nanograins, dislocation hardening, and hardening by the uniform distribution of dual-size broken [CrMoFe]-rich dendrite fragments with semicoherent interphases [1,18,59–61].

According to Table 2 and Fig. 6, the wear rate and friction coefficient of the CCDF-processed $Fe_{30}Ni_{25}Cr_{25}Mo_{10}Al_{10}$ alloy, i.e., (0.8 ± 0.1) × 10^{-5} mm^3. N^{-1}.m^{-1} and 0.31, are significantly lower than those of the as-homogenized state ((3.1 ± 0.1) × 10^{-5} mm^3. N^{-1}.m^{-1} and 0.64) and as-homogenized $Fe_{25}Ni_{25}Cr_{25}Mo_{25}$ alloy ((4.3 ± 0.1) × 10^{-5} mm^3. N^{-1}.m^{-1} and 0.71). This can be attributed to the surface strengthening of the CCDF-processed alloy through strain hardening (i.e., an increase in the dislocation density and their interactions) [62], the volume fraction of nanograins [63], the reinforcing role of broken [CrMoFe]-rich dendrite fragments in the matrix (i.e., additional strain hardening) [64], and the uniformity of the fine dendrite distribution in the matrix [21,58,65]. Therefore, it can be concluded that the wear resistance properties of the as-homogenized $Fe_{30}Ni_{25}Cr_{25}Mo_{10}Al_{10}$ alloy significantly improves after CCDF processing.

The crystallographic texture of metals and alloys can affect their tribological characteristic. During sliding contact, the interfacial shear stresses of the alloys adapt, resulting in a reduction in wear rate by forming nanostructured tribo-layers, shear bands, and basal texture alignment parallel to the sliding direction [66,67]. For instance, Yu et al. [68] found that the presence of the Rotated Cube {001}<110> and Cube {001}<100> texture components in low-carbon micro-alloyed steel during hot rolling significantly enhanced tribological performance. In the present work, the Rotated Cube {001}<110> component was observed in the sixth CCDF pass (see Fig. 5). Consequently, it can be concluded that the presence of Rotated Cube {001}<110> component with a maximum intensity of 2.7 × R can enhance the wear resistance

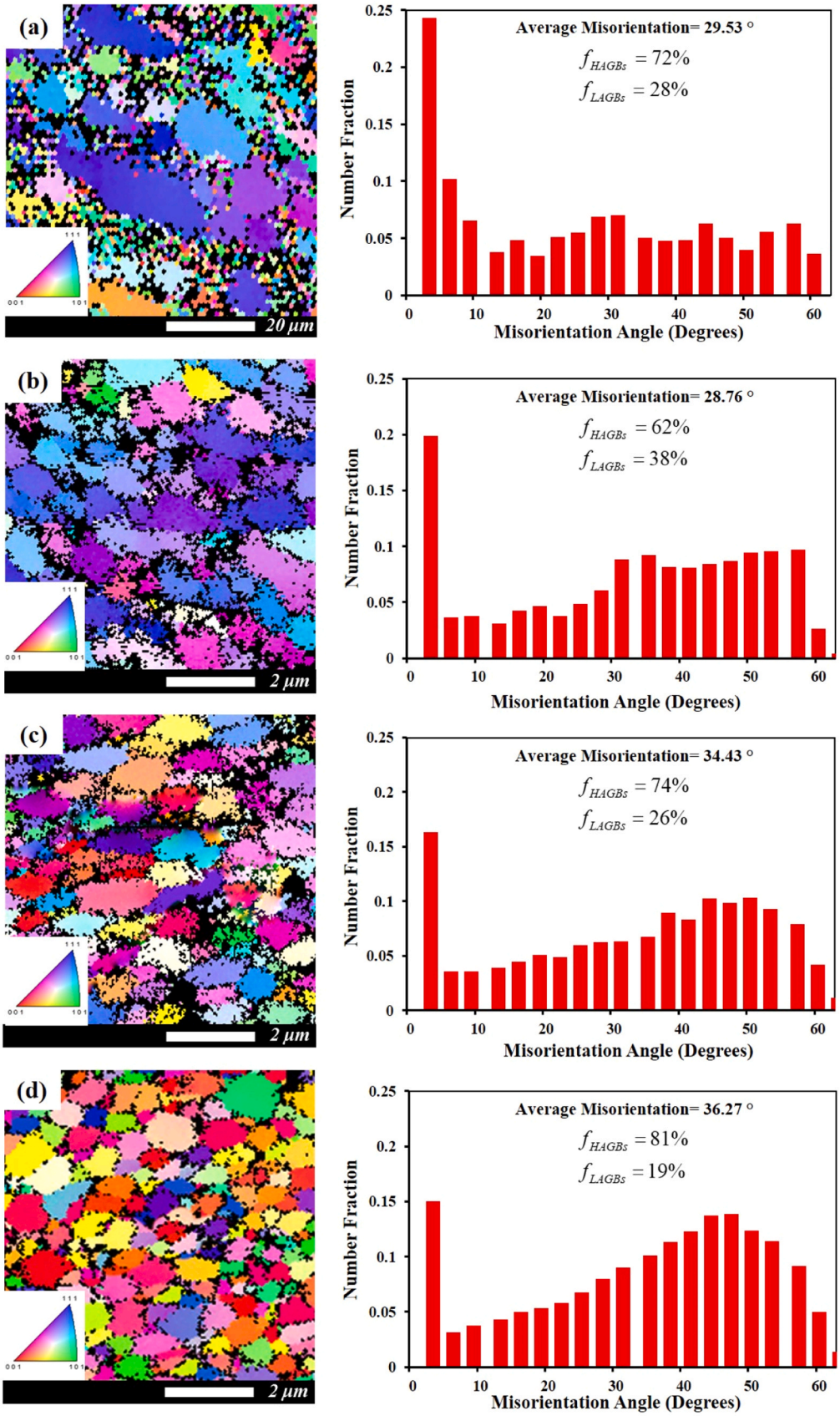

Fig. 4. EBSD inverse pole figure (IPF) maps and misorientation angle distribution of the $Fe_{30}Ni_{25}Cr_{25}Mo_{10}Al_{10}$ alloy: (a) before CCDF and after (b) two, (c) four, and (d) six CCDF passes.

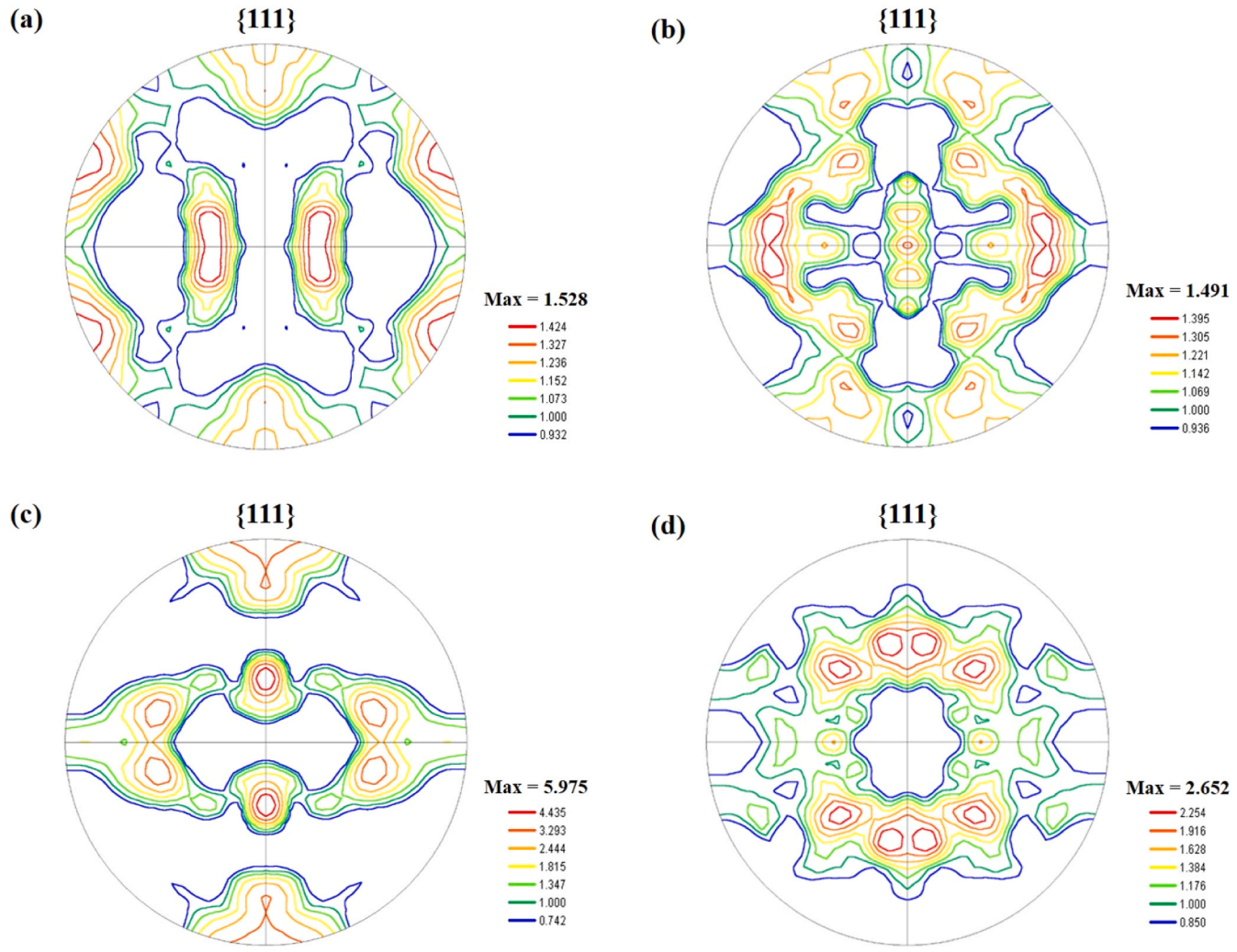

Fig. 5. {111} Pole figure of the $Fe_{30}Ni_{25}Cr_{25}Mo_{10}Al_{10}$ alloy: (a) before CCDF and after (b) two, (c) four, and (d) six CCDF passes.

Table 2
Calculated values of microhardness, wear rate, and friction coefficient for the as-homogenized and CCDF-processed alloys.

HEA	Microhardness (HV)	Wear rate ($mm^3.N^{-1}.m^{-1}$)	Friction coefficient
As-homogenized $Fe_{25}Ni_{25}Cr_{25}Mo_{25}$	195	$(4.3 \pm 0.1) \times 10^{-5}$	0.71
As-homogenized $Fe_{30}Ni_{25}Cr_{25}Mo_{10}Al_{10}$	412	$(3.1 \pm 0.1) \times 10^{-5}$	0.64
CCDF-processed $Fe_{30}Ni_{25}Cr_{25}Mo_{10}Al_{10}$	974	$(0.8 \pm 0.1) \times 10^{-5}$	0.31

properties of the CCDF-processed $Fe_{30}Ni_{25}Cr_{25}Mo_{10}Al_{10}$ alloy.

Fig. 7 illustrates the worn surface morphologies of the as-homogenized $Fe_{40}Ni_{25}Cr_{25}Mo_{25}$ alloy, the as-homogenized $Fe_{30}Ni_{25}Cr_{25}Mo_{10}Al_{10}$ alloy, and the CCDF-processed alloy after six passes. The as-homogenized alloys exhibit significant adhesive and surface damage, leading to a higher extent of delamination. However, the depth of grooves and adhesive wear are notably lower in the $Fe_{30}Ni_{25}Cr_{25}Mo_{10}Al_{10}$ alloy compared to the $Fe_{40}Ni_{25}Cr_{25}Mo_{25}$ alloy, as depicted in Fig. 7(a) and (b). In Fig. 7(c), the worn surface of the CCDF-processed $Fe_{30}Ni_{25}Cr_{25}Mo_{10}Al_{10}$ alloy exhibits shallow wear grooves, indicating both abrasive and adhesive wear. Furthermore, there is a significant reduction in plastic deformation, depth of grooves, degree of delamination, and adhesive wear in the CCDF-processed alloy when compared to the homogenized states.

Achieving exceptional grain refinement using SPD processing is crucial for enhancing the hardness and wear resistance of metals and alloys [69–75]. The wear volume decreases with increasing hardness, according to Archard's law [76] of wear. After CCDF, the size of the grains decreases (Fig. 4 and Table 2), contributing to increased hardness of the HEAs and decreased wear volume. Additionally, the morphological characteristics such as as-cast dendrites, volume fraction, size distribution, crystallographic texture, and other characteristics play a significant role in influencing the mechanical and wear properties of the HEAs. In the present work, grain refinement achieved via CCDF processing can effectively reduce adhesive wear and enhance the resistance to adhesion of the cost-effective $Fe_{30}Ni_{25}Cr_{25}Mo_{10}Al_{10}$ alloy by influencing plastic deformation (see Fig. 7). The findings of this research indicate that CCDF processing of HEAs offers a promising approach for the cost-effective development of NsHEAs. While techniques like ECA-P/ECAE and HPT techniques have not yet reported success in improving the wear resistance of HEAs, our results strongly suggest that CCDF processing has the potential to achieve these enhancements.

4. Conclusions

This study presents the processing of a cost-effective novel $Fe_{30}Ni_{25}Cr_{25}Mo_{10}Al_{10}$ high-entropy alloy through cyclic closed-die

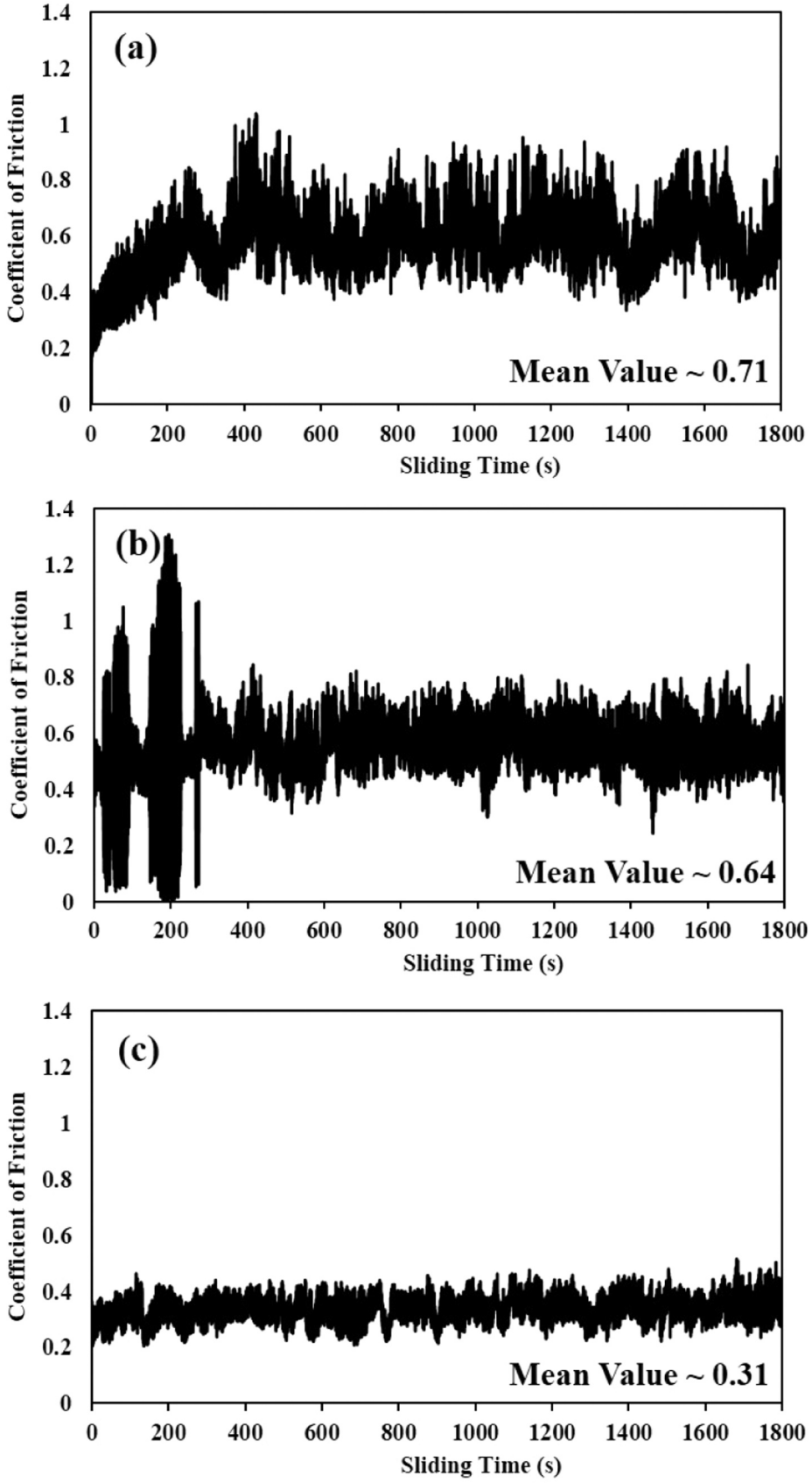

Fig. 6. Variation of coefficient of friction with sliding time for (a) as-homogenized $Fe_{25}Ni_{25}Cr_{25}Mo_{25}$ alloy, (b) as-homogenized $Fe_{30}Ni_{25}Cr_{25}Mo_{10}Al_{10}$ alloy, and (c) CCDF-processed $Fe_{30}Ni_{25}Cr_{25}Mo_{10}Al_{10}$ alloy.

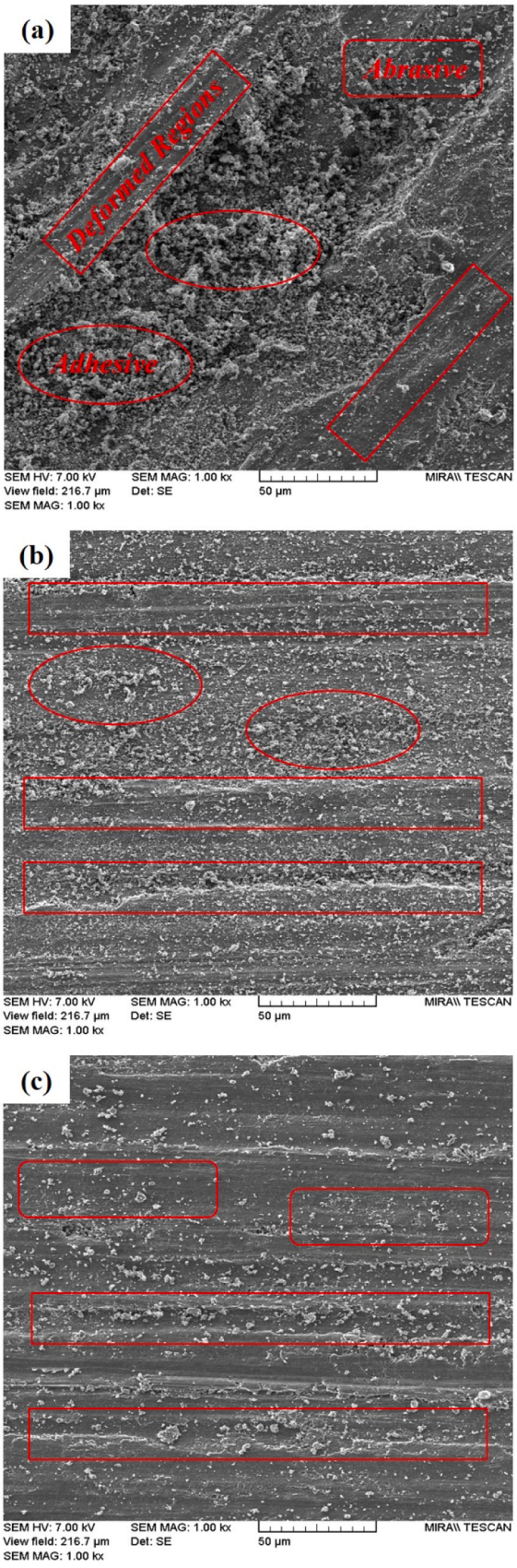

Fig. 7. Morphologies of worn surfaces of the (a) as-homogenized $Fe_{25}Ni_{25}Cr_{25}Mo_{25}$ alloy, (b) as-homogenized $Fe_{30}Ni_{25}Cr_{25}Mo_{10}Al_{10}$ alloy, and (c) CCDF-processed $Fe_{30}Ni_{25}Cr_{25}Mo_{10}Al_{10}$ alloy.

forging (CCDF) to enhance its hardness and wear resistance properties. The increase in CCDF passes leads to exceptional grain refinement, formation of homogenous equiaxed nanograins, fragmentation of [CrMoFe]-rich dendrites, and their efficient distribution in the matrix. Texture analysis reveals that the reduction in texture intensity during final passes is linked to the development of equiaxed nanograins and the redundant shear strain imposed during the CCDF processing. Also, the Rotated Cube {001}<110>, S {123}<634>, and Dillamore {4 4 11}<11 11 8> are the main texture components in the $Fe_{30}Ni_{25}Cr_{25}Mo_{10}Al_{10}$ alloy after six CCDF passes. The CCDF-processed $Fe_{30}Ni_{25}Cr_{25}Mo_{10}Al_{10}$ alloy demonstrates the highest microhardness (~ 974 HV) and the lowest wear rate (~ $(0.8 \pm 0.1) \times 10^{-5}$ $mm^3.N^{-1}.m^{-1}$). Furthermore, the development of a strong Rotated Cube {001}<110> texture component significantly contributes to the enhanced wear resistance in the cost-effective Fe-based HEAs. Therefore, it is reasonable to highlight the potential industrial applications of these cost-effective nano-structured HEAs.

CRediT authorship contribution statement

Majid Naseri: Conceptualization, Investigation, Validation, Writing – original draft, Writing – review & editing, Funding acquisition. **Alena Myasnikova**: Investigation. **Davood Gholami**: Investigation, Validation. **Omid Imantalab**: Investigation, Validation, Writing – review & editing. **Dmitry Mikhailov**: Investigation, Validation. **Mostafa Amra**: Investigation, Writing – original draft, Writing – review & editing. **Nataliya Shaburova**: Investigation. **Milena Efimova**: Investigation. **Aleksandr Orlov**: Investigation. **Seyedmehdi Hosseini**: Writing – original draft, Writing – review & editing. **Yong-Cheng Lin**: Writing – review & editing. **Abdel-Hamid I Mourad**: Writing – review & editing. **Evgeny Trofimov**: Writing – review & editing.

Declaration of Competing Interest

The authors declare that they have no known competing financial interests or personal relationships that could have appeared to influence the work reported in this paper.

Acknowledgment

The study was supported by the Russian Science Foundation, project No. 24–29–00740, https://rscf.ru/en/project/24–29-00740/.

References

[1] M.J. Sohrabi, A. Kalhor, H. Mirzadeh, K. Rodak, H.S. Kim, Tailoring the strengthening mechanisms of high-entropy alloys toward excellent strength-ductility synergy by metalloid silicon alloying: a review, Prog. Mater. Sci. 144 (2024) 101295.
[2] H. Khodashenas, H. Mirzadeh, Post-processing of additively manufactured high-entropy alloys - A review, J. Mater. Res. Technol. 21 (2022) 3795–3814.
[3] Y. Wang, J. Zhang, T. Wu, G. Huang, An all-around way to analyze the corrosion behavior and the potential applications of high-entropy alloys coating, Ceram. Int. 50 (4) (2024) 5893–5913.
[4] V. Verma, C.H. Belcher, D. Apelian, E.J. Lavernia, Diffusion in high entropy alloy systems – a review, Prog. Mater. Sci. 142 (2024) 101245.
[5] B. Cantor, I. Chang, P. Knight, A. Vincent, Microstructural development in equiatomic multicomponent alloys, Mater. Sci. Eng.: A 375 (2004) 213–218.
[6] J.W. Yeh, S.K. Chen, S.J. Lin, J.Y. Gan, T.S. Chin, T.T. Shun, C.H. Tsau, S.Y. Chang, Nanostructured high-entropy alloys with multiple principal elements: novel alloy design concepts and outcomes, Adv. Eng. Mater. 6 (5) (2004) 299–303.
[7] A.H. Lashkari, A.O. Moghaddam, M. Naseri, A. Shokuhfar, Synthesis and characterization of high entropy carbide-MAX two-phase composites, J. Mater. Res. Technol. 24 (2023) 5024–5031.
[8] A.O. Moghaddam, R. Fereidonnejad, M. Naseri, N. Shaburova, D. Mikhailov, S. Uporov, E. Trofimov, Synthesis and characterization of novel high entropy Heusler intermetallics, Intermetallics 159 (2023) 107917.
[9] E. Trofimov, A.O. Moghaddam, O. Zaitseva, R. Fereidonnejad, M. Naseri, N. Shaburova, D. Mikhailov, Synthesis and characterization of intermetallic compounds with one medium-or high-entropy sublattice occupied by p-block elements, Mater. Chem. Phys. 301 (2023) 127596.

[10] S.H. Shim, H. Pouraliakbar, Y.K. Kim, B.J. Lee, V. Fallah, Y.K. Kim, K.R. Lim, Y. S. Na, S.I. Hong, Exploring the impact of heat treatment on the transformation of hierarchical microstructure and mechanical properties in a non-equiatomic CrMnFeNiCu high-entropy alloy with a reversible structure, J. Alloy. Compd. 969 (2023) 172514.

[11] J. Chen, Z. Fang, P. Wu, H. Liu, L. Hu, T. Tuoliken, Z. Li, Q. Sun, Strengthening a non-equiatomic quaternary high-entropy alloy via concurrent gradient structures of nanotwin and dislocation cell, Mater. Sci. Eng.: A 909 (2024) 146816.

[12] R. Yin, P.J. Masset, K.F. Gan, L.G. Zhang, L.B. Liu, Minor element doping effects on microstructure and mechanical properties of a non-equiatomic FeNiCoCr high-entropy alloy, Mater. Charact. 215 (2024) 114178.

[13] M. Lee, G. Choi, K. Lee, TRIP behavior of non-equiatomic $Co_{40}Cr_{20}Ni_{15}Fe_{15}Mo_{10}$ high entropy alloys, Int. J. Refract. Met. Hard Mater. 115 (2023) 106288.

[14] Y. Lu, Y. Dong, S. Guo, L. Jiang, H. Kang, T. Wang, B. Wen, Z. Wang, J. Jie, Z. Cao, A promising new class of high-temperature alloys: eutectic high-entropy alloys, Sci. Rep. 4 (1) (2014) 6200.

[15] L. Yu, X. Ye, D. Fang, M. Liu, H. Guo, S. Wang, G. Zhao, B. Li, H. Wu, Precise design strategy of FeNiCrMo eutectic high-entropy alloys, J. Mater. Res. Technol. 21 (2022) 3207–3219.

[16] X. Chen, J.Q. Qi, Y.W. Sui, Y.Z. He, F.X. Wei, Q.K. Meng, Z. Sun, Effects of aluminum on microstructure and compressive properties of Al-Cr-Fe-Ni eutectic multi-component alloys, Mater. Sci. Eng.: A 681 (2017) 25–31.

[17] Y. Lu, M. Zhang, L. Zhang, P. Yu, R. Li, X. Liu, Y. Zhang, G. Li, Cobalt-element-free eutectic medium-entropy alloys with superior mechanical performance and processability, Mater. Sci. Eng.: A 801 (2021) 140421.

[18] M.J. Sohrabi, M.S. Mehranpour, J.H. Lee, A. Heydarinia, H. Mirzadeh, H.S. Kim, Overcoming strength-ductility trade-off in Si-containing transformation-induced plasticity high-entropy alloys via metastability engineering, Mater. Sci. Eng.: A 908 (2024) 146766.

[19] M. Naseri, S. Pratskova, O. Imantalab, D. Gholami, D. Mikhailov, M.M. Dana, N. Shaburova, A. Pellenen, A.H.I. Mourad, A. Myasnikova, Y.-C. Lin, M. Samodurova, E. Trofimov, Achieving ultrafine lamellar structure and exceptional electrochemical properties of $Fe_{35}Mn_{27}Ni_{28}Co_5Cr_5$ high-entropy alloy through severe cold rolling process, Mater. Today Commun. 39 (2024) 109053.

[20] M. Naseri, A.O. Moghaddam, N. Shaburova, D. Mikhailov, D. Gholami, A.H. I. Mourad, A. Pellenen, E. Trofimov, Upgrading the strength-ductility trade-off and wear resistance of $Al_{0.25}CoCrFeNiCu$ and $Al_{0.45}CoCrFeNiSi_{0.45}$ high-entropy alloys through severe cold rolling process, Mater. Today Commun. 38 (2024) 108036.

[21] M. Naseri, A.O. Moghaddam, N. Shaburova, D. Gholami, A. Pellenen, E. Trofimov, Ultrafine lamellar microstructures for enhancing strength-ductility synergy in high-entropy alloys via severe cold rolling process, J. Alloy. Compd. 965 (2023) 171385.

[22] M. Naseri, A.O. Moghadam, M. Anandkumar, S. Sudarsan, E. Bodrov, M. Samodurova, E. Trofimov, Enhancing the mechanical properties of high-entropy alloys through severe plastic deformation: a review, J. Alloy. Metall. Syst. (2024) 100054.

[23] H. Jiang, Q. Gong, M. Peterlechner, L. Daum, H. Rösner, G. Wilde, Hardness and microstructural evolution of CoCrFeNi high-entropy alloys during severe plastic deformation, Mater. Sci. Eng.: A (2024) 146758.

[24] S.N. Kumaran, S.K. Sahoo, C. Haase, L.A. Barrales-Mora, L.S. Toth, Nano-structuring of a high entropy alloy by severe plastic deformation: Experiments and crystal plasticity simulations, Acta Mater. 250 (2023) 118814.

[25] K.W. Park, W.J. Kim, Recovery stress and strain behavior of $Cr_{20}Mn_{20}Fe_{20}Co_{35}Ni_5$ high entropy alloy deformed via severe plastic deformation, Mater. Charact. 197 (2023) 112641.

[26] Y.L. Bian, Z.D. Feng, N.B. Zhang, Y.X. Li, X.F. Wang, B.B. Zhang, Y. Cai, L. Lu, S. Chen, X.H. Yao, S.N. Luo, Ultrafast severe plastic deformation in high-entropy alloy $Al_{0.1}CoCrFeNi$ via dynamic equal channel angular pressing, Mater. Sci. Eng.: A 847 (2022) 143221.

[27] J. Gubicza, P.T. Hung, M. Kawasaki, J.K. Han, Y. Zhao, Y. Xue, J.L. Lábár, Influence of severe plastic deformation on the microstructure and hardness of a CoCrFeNi high-entropy alloy: a comparison with CoCrFeNiMn, Mater. Charact. 154 (2019) 304–314.

[28] A. Keyvani, M. Naseri, O. Imantalab, D. Gholami, K. Babaei, A. Fattah-alhosseini, Microstructural characterization and electrochemical behavior of nano/ultrafine grained pure copper through constrained groove pressing (CGP), J. Mater. Res. Technol. 11 (2021) 1918–1931.

[29] M. Naseri, M. Reihanian, E. Borhani, EBSD characterization of nano/ultrafine structured Al/Brass composite produced by severe plastic deformation, J. Ultra Graine Nanostruct. Mater. 51 (2) (2018) 123–138.

[30] M. Naseri, E. Borhani, O. Imantalab, H.W. Jang, M. Shokouhimehr, A. Fattah-alhosseini, Correlation between crystallographic texture and electrochemical behavior of nano/ultrafine-grained AA2024 alloy processed by accumulative roll bonding process, J. Mater. Res. Technol. 18 (2022) 4256–4266.

[31] D. Gholami, O. Imantalab, M. Naseri, S. Vafaeian, A. Fattah-alhosseini, Assessment of microstructural and electrochemical behavior of severely deformed pure copper through equal channel angular pressing, J. Alloy. Compd. 723 (2017) 856–865.

[32] M. Naseri, D. Gholami, O. Imantalab, F. Attarzadeh, A. Fattah-alhosseini, Effect of grain refinement on mechanical and electrochemical properties of severely deformed pure copper through equal channel angular pressing, Mater. Res. Express 5 (7) (2018) 076504.

[33] M. Alvand, M. Naseri, E. Borhani, H. Abdollah-Pour, Nano/ultrafine grained AA2024 alloy processed by accumulative roll bonding: a study of microstructure, deformation texture and mechanical properties, J. Alloy. Compd. 712 (2017) 517–525.

[34] M. Reihanian, M. Naseri, M. Jalili Shahmansouri, Effect of the particle size on the deformation and fracture behavior of Al/4vol% Al_2O_3 composite produced by accumulative roll bonding (ARB), Iran. J. Mater. Form. 2 (2) (2015) 14–26.

[35] F. Otto, A. Dlouhý, C. Somsen, H. Bei, G. Eggeler, E.P. George, The influences of temperature and microstructure on the tensile properties of a CoCrFeMnNi high-entropy alloy, Acta Mater. 61 (15) (2013) 5743–5755.

[36] S. Hu, T. Li, Q. Li, D. Liu, Microstructure evolution, deformation mechanism, and mechanical properties of biomedical TiZrNb medium entropy alloy processed using equal channel angular pressing, Intermetallics 151 (2022) 107725.

[37] S. Picak, T. Wegener, S.V. Sajadifar, C. Sobrero, J. Richter, H. Kim, T. Niendorf, I. Karaman, On the low-cycle fatigue response of CoCrNiFeMn high entropy alloy with ultra-fine grain structure, Acta Mater. 205 (2021) 116540.

[38] S. Picak, H.C. Yilmaz, I. Karaman, Simultaneous deformation twinning and martensitic transformation in CoCrFeMnNi high entropy alloy at high temperatures, Scr. Mater. 202 (2021) 113995.

[39] J. Hidalgo-Jimenez, J.M. Cubero-Sesin, K. Edalati, S. Khajavi, J. Huot, Effect of high-pressure torsion on first hydrogenation of Laves phase $Ti_{0.5}Zr_{0.5}(Mn_{1-x}Fe_x)Cr_1$ ($x = 0$, 0.2 and 0.4) high entropy alloys, J. Alloy. Compd. 969 (2023) 172243.

[40] R. Sonkusare, N.P. Gurao, K. Biswas, J. Basu, S. Sen, K.G. Pradeep, M. Praveena, S. Bhowmick, S. Bhowmick, A. Kilmametov, M. Palit, Micro-mechanisms of deformation and strengthening during high pressure torsion of CoCuFeMnNi high entropy alloy, Materialia 32 (2023) 101916.

[41] X. Liu, H. Ding, Y. Huang, X. Bai, Q. Zhang, H. Zhang, T.G. Langdon, J. Cui, Evidence for a phase transition in an $AlCrFe_2Ni_2$ high entropy alloy processed by high-pressure torsion, J. Alloy. Compd. 867 (2021) 159063.

[42] W. Guo, Q. Wang, B. Ye, H. Zhou, Microstructure and mechanical properties of AZ31 magnesium alloy processed by cyclic closed-die forging, J. Alloy. Compd. 558 (2013) 164–171.

[43] W. Liao, B. Ye, L. Zhang, H. Zhou, W. Guo, Q. Wang, W. Li, Microstructure evolution and mechanical properties of SiC nanoparticles reinforced magnesium matrix composite processed by cyclic closed-die forging, Mater. Sci. Eng.: A 642 (2015) 49–56.

[44] W. Guo, Q. Wang, B. Ye, H. Zhou, Enhanced microstructure homogeneity and mechanical properties of AZ31–Si composite by cyclic closed-die forging, J. Alloy. Compd. 552 (2013) 409–417.

[45] A.K. Ghosh, Method of producing a fine grain aluminum alloy using three axes deformation, Google Pat. (1988).

[46] G. Sheng, C.T. Liu, Phase stability in high entropy alloys: Formation of solid-solution phase or amorphous phase, Prog. Nat. Sci.: Mater. Int. 21 (6) (2011) 433–446.

[47] S. Guo, C. Ng, J. Lu, C. Liu, Effect of valence electron concentration on stability of FCC or BCC phase in high entropy alloys, J. Appl. Phys. 109 (10) (2011).

[48] P. Edalati, A. Mohammadi, M. Ketabchi, K. Edalati, Ultrahigh hardness in nanostructured dual-phase high-entropy alloy AlCrFeCoNiNb developed by high-pressure torsion, J. Alloy. Compd. 884 (2021) 161101.

[49] R.Z. Valiev, R.K. Islamgaliev, I.V. Alexandrov, Bulk nanostructured materials from severe plastic deformation, Prog. Mater. Sci. 45 (2) (2000) 103–189.

[50] J.C. Cheng, N. Li, P. Xia, H.L. Qin, F. Zhao, Q.C. Liu, Effect of deformation heterogeneity on development of geometrically necessary dislocation density in heterogeneous-structured CrMnFeCoNi high-entropy alloy, Mater. Lett. 358 (2024) 135834.

[51] T. Shu, N. Hu, F. Liu, G.J. Cheng, Nanoparticles induced intragranular and dislocation substructures in powder bed fusion for strengthening of high-entropy-alloy, Mater. Sci. Eng.: A 878 (2023) 145110.

[52] M. Naseri, M. Reihanian, E. Borhani, A new strategy to simultaneous increase in the strength and ductility of AA2024 alloy via accumulative roll bonding (ARB), Mater. Sci. Eng.: A 656 (2016) 12–20.

[53] M. Naseri, M. Reihanian, E. Borhani, Effect of strain path on microstructure, deformation texture and mechanical properties of nano/ultrafine grained AA1050 processed by accumulative roll bonding (ARB), Mater. Sci. Eng.: A 673 (2016) 288–298.

[54] Y. Bian, Z. Feng, N. Zhang, Y. Li, X. Wang, B. Zhang, Y. Cai, L. Lu, S. Chen, X. Yao, Ultrafast severe plastic deformation in high-entropy alloy $Al_{0.1}CoCrFeNi$ via dynamic equal channel angular pressing, Mater. Sci. Eng.: A 847 (2022) 143221.

[55] H. Shahmir, T. Mousavi, J. He, Z. Lu, M. Kawasaki, T.G. Langdon, Microstructure and properties of a CoCrFeNiMn high-entropy alloy processed by equal-channel angular pressing, Mater. Sci. Eng.: A 705 (2017) 411–419.

[56] C. Duan, A. Kostka, X. Li, Z. Peng, P. Kutlesa, R. Pippan, E. Werner, Deformation-induced homogenization of the multi-phase senary high-entropy alloy MoNbTaTiVZr processed by high-pressure torsion, Mater. Sci. Eng.: A 871 (2023) 144923.

[57] S. Park, H. Nam, Y. Lee, N. Park, S. Hong, Y. Na, C. Park, N. Kang, Enhancement of hardness and yield strength induced by Cu-rich phase and its effect at cryogenic temperature on gas tungsten arc welds of ferrous medium-entropy alloy, Met. Mater. Int. 29 (8) (2023) 2316–2330.

[58] Z. Wu, M. Chen, B. Li, M. Lv, R. Zheng, Y. Yang, X. Tan, H. Xu, A novel formation and structure evolution of Cu-rich precipitates in FeCoNiCuAl high-entropy alloy, Mater. Charact. 191 (2022) 112161.

[59] W. Ji, M.S. Wu, Inhibiting the inverse Hall-Petch behavior in CoCuFeNiPd high-entropy alloys with short-range ordering and grain boundary segregation, Scr. Mater. 221 (2022) 114950.

[60] S. Yoshida, T. Ikeuchi, T. Bhattacharjee, Y. Bai, A. Shibata, N. Tsuji, Effect of elemental combination on friction stress and Hall-Petch relationship in face-centered cubic high/medium entropy alloys, Acta Mater. 171 (2019) 201–215.

[61] A. Fattah-alhosseini, M. Naseri, O. Imantalab, D. Gholami, M. Haghshenas, The passive film characteristics of cold deformed pure copper, J. Mater. Eng. Perform. 25 (11) (2016) 4741–4749.
[62] A.P. Zhilyaev, T.G. Langdon, Using high-pressure torsion for metal processing: Fundamentals and applications, Prog. Mater. Sci. 53 (6) (2008) 893–979.
[63] R.Z. Valiev, Y. Estrin, Z. Horita, T.G. Langdon, M.J. Zechetbauer, Y.T. Zhu, Producing bulk ultrafine-grained materials by severe plastic deformation, JOM 58 (2006) 33–39.
[64] Z. Li, K.G. Pradeep, Y. Deng, D. Raabe, C.C. Tasan, Metastable high-entropy dual-phase alloys overcome the strength–ductility trade-off, Nature 534 (7606) (2016) 227–230.
[65] M. Naseri, A.O. Moghaddam, S. Lezhnev, N. Shaburova, A. Pellenen, E. Bodrov, E. Panin, M. Samodurova, E. Trofimov, Exploring strengthening mechanisms of ultrafine-grained $Fe_{35}Mn_{27}Ni_{28}Co_5Cr_5$ high-entropy alloy processed by severe cold rolling process, J. Chem. Technol. Metall. 59 (3) (2024) 653–660.
[66] H. Mohseni, P. Nandwana, A. Tsoi, R. Banerjee, T. Scharf, In situ nitrided titanium alloys: Microstructural evolution during solidification and wear, Acta Mater. 83 (2015) 61–74.
[67] R. Jamaati, M. Naseri, M.R. Toroghinejad, Wear behavior of nanostructured Al/Al_2O_3 composite fabricated via accumulative roll bonding (ARB) process, Mater. Des. 59 (2014) 540–549.
[68] X. Yu, Z. Jiang, J. Zhao, D. Wei, J. Zhou, C. Zhou, Q. Huang, The role of oxide-scale microtexture on tribological behaviour in the nanoparticle lubrication of hot rolling, Tribology Int. 93 (2016) 190–201.
[69] T.A. Yilmaz, Y. Totik, G.M. Lule Senoz, B. Bostan, Microstructure evolution and wear properties of ECAP-treated Al-Zn-Mg alloy: Effect of route, temperature and number of passes, Mater. Today Commun. 33 (2022) 104628.
[70] M. Elhefnawey, G.L. Shuai, Z. Li, D.T. Zhang, M.M. Tawfik, L. Li, On achieving ultra-high strength and improved wear resistance in Al–Zn–Mg alloy via ECAP, Tribology Int. 163 (2021) 107188.
[71] E. Avcu, The influences of ECAP on the dry sliding wear behaviour of AA7075 aluminium alloy, Tribology Int. 110 (2017) 173–184.
[72] A.V. Filippov, S.Y. Tarasov, S.V. Fortuna, O.A. Podgornykh, N.N. Shamarin, V. E. Rubtsov, Microstructural, mechanical and acoustic emission-assisted wear characterization of equal channel angular pressed (ECAP) low stacking fault energy brass, Tribology Int. 123 (2018) 273–285.
[73] M.I. Abd El Aal, N. El Mahallawy, F.A. Shehata, M. Abd El Hameed, E.Y. Yoon, H. S. Kim, Wear properties of ECAP-processed ultrafine grained Al–Cu alloys, Mater. Sci. Eng.: A 527 (16) (2010) 3726–3732.
[74] P. Seenuvasaperumal, K. Doi, D.A. Basha, A. Singh, A. Elayaperumal, K. Tsuchiya, Wear behavior of HPT processed UFG AZ31B magnesium alloy, Mater. Lett. 227 (2018) 194–198.
[75] H. Kato, Y. Todaka, M. Umemoto, M. Haga, E. Sentoku, Sliding wear behavior of sub-microcrystalline pure iron produced by high-pressure torsion straining, Wear 336-337 (2015) 58–68.
[76] J. Archard, Contact and rubbing of flat surfaces, J. Appl. Phys. 24 (8) (1953) 981–988.